A simplified method for the detection of convection using high resolution imagery from GOES-16

Yoonjin Lee[1], Christian D. Kummerow[1,2], Milija Zupanski[2]

[1]Department of Atmospheric Science, Colorado state university, Fort Collins, CO 80521, USA
5 [2]Cooperative Institute for Research in the Atmosphere, Colorado state university, Fort Collins, CO 80521, USA

Correspondence to: Yoonjin Lee (ylee@atmos.colostate.edu)

Abstract. The ability to detect convective regions and assimilating the proper heating in these regions is the most important skill in forecasting severe weather systems. Since radars are most directly related to precipitation and are available in high temporal resolution, their data are often used for both detecting convection and estimating latent heating. However, radar data 10 are limited to land areas, largely in developed nations, and early convection is not detectable from radars until drops become large enough to produce significant echoes. Visible and Infrared sensors on a geostationary satellite can provide data that are less sensitive to drop size, but they also have shortcomings: their information is almost exclusively from the cloud top. Relatively new geostationary satellites, GOES-16 and GOES-17, along with Himawari-8, can make up for some of this lack of vertical information through the use of very high spatial and temporal resolutions. This study develops two algorithms to 15 detect convection at different life stages using 1-minute GOES-16 ABI data. Two case studies are used to explain the two methods, followed by results applied to one month of data over the contiguous United States. Vertically growing clouds in early stages were detected using decreases in brightness temperatures over ten minutes. Of the detected clouds, the method correctly identifies 71.0% to be convective. For mature convective clouds which no longer show decreases in brightness temperature, the lumpy texture, and rapid temporal evolution can be observed using 1-minute high spatial resolution 20 reflectance data. The algorithm that uses texture and evolution for mature convection detects with an accuracy of 85.8%. 54.7% of clouds that are identified as convective by the ground-based radars are missed by the satellite. These convective clouds are largely under optically thick cloud shields.

1 Introduction

While weather forecast models have improved tremendously throughout the decades (Bauer et al., 2015), local scale 25 phenomena such as convection remain challenging (Yano et al., 2018). Precipitation is especially hard to predict as numerical models struggle with initiating convection in the right location and intensity. To address this issue in short term predictions, many models now assimilate all-sky radiances and precipitation-related products where available. (Bonavita et al., 2017; Benjamin et al., 2016; Migliorini et al., 2018; Geer et al., 2017; Jones et al., 2016) In some forecast models such as the High Resolution Rapid Refresh (HRRR) model in the United States, latent heating is added, along with precipitation affected

30 radiances, to adjust model dynamics to correspond to the observed convection (Benjamin et al., 2016). Given the rather recent emergence of these techniques, and the complex structure of latent heating (Tao et al., 1990), there is not yet a standard method of how best to assimilate this heating. Nor is there a direct measurement of latent heating, although it is generally accepted that convective regions have positive heating throughout the vertical column while stratiform regions have negative heating in the lower layers and positive heating aloft. Because local scale phenomena tend to develop first by

35 convective clouds before detraining stratiform precipitation, it is critical to correctly detect convective regions.

Convection is classically defined from in-cloud vertical air motions (Steiner et al., 1995). However, since vertical velocity is rarely measured directly, the radar community initially adopted radar reflectivity thresholds to define convection and distinguish it from stratiform precipitation (Churchill and Houze, 1984; Steiner et al., 1995). One problem with using

40 reflectivity threshold is its sensitivity to the selected threshold for convection. If the threshold is set high, convective regions where precipitation has just begun are not captured, while a threshold that is set too low will misclassify some stratiform regions as convective. To address this issue, Churchill and Houze (1984) separated precipitation types using the horizontal structure of precipitation fields (Steiner et al., 1995). They classified a grid as convective if the grid had rain rates twice as high as the average taken over surrounding grids or had reflectivity over 40dBZ (~ 20 mm h^{-1}). Steiner et al. (1995) refined

45 this method with three criteria: intensity, peakedness, and surrounding area. They used the same threshold of 40dBZ for intensity, but used variable thresholds for reflectivity differences between convective cores and surrounding areas depending on the mean background reflectivity. Nonetheless, stratiform regions sometimes can have reflectivity values greater than 40dBZ. Zhang et al. (2008) used two reflectivity criteria for convective precipitation-namely that the reflectivity be greater than 50dBZ at any height and greater than 30dBZ at -10°C or higher. Zhang and Qi (2010) used a vertically integrated liquid

50 water field and had a single threshold of 6.5kg m^{-2}. Qi et al. (2013) developed a new algorithm that combined two previous methods from Zhang et al. (2008) and Zhang and Qi (2010). By combining these two methods and modifying the thresholds, they were able to decrease misclassification of stratiform regions with strong bright band features, but could still miss some convective regions in their initial stage due to a high reflectivity threshold. The HRRR model uses a much lower reflectivity threshold of 28dBZ to detect convective regions and assigns a heating increment (Weygandt et al., 2016). While this is

55 significantly lower than the thresholds discussed above, its primary purpose is to initiate convection where there is significant echo present, while relying on the model physics to assign the proper precipitation type.

While radars have been the preferred method for detecting convection, they are not the only instruments available. Visible (VIS) and infrared (IR) radiances also contain some information, although largely limited to cloud top properties. Convection

60 detection algorithms using VIS and IR sensors exist for both convective initiation (CI) and mature stages. At the initial stages of convection, cloud tops grow vertically, and most algorithms use decreased cloud top temperature from the growth (related to the in-cloud vertical velocity) to detect convective regions. The cloud-top-cooling (CTC) algorithm (Sieglaff et al., 2011; Sieglaff et al., 2014) calculates averaged brightness temperature (T_b) in a small region and finds pixels with cooling trends.

The algorithm eliminates pixels with false cooling from horizontal cloud advection, thin cirrus motion, and complex
multilayer cloud scenes and only detects vertically growing clouds (Sieglaff et al., 2011). Another algorithm by Mecikalski
and Bedka (2006) tracks clouds and determines if the clouds have a high likelihood for CI by using spectral thresholds in
interest fields. Interest fields include the temporal trend of T_b at 10.7µm or temporal trends of differences in T_b between two
channels that are sensitive to water vapor or cloud water (Mecikalski and Bedka, 2006).

Convective clouds in their mature stage cannot be detected by the abovementioned algorithms as their cloud tops do not grow
much in the vertical, and therefore do not exhibit cooling in the mean T_b is observed over time. "Lumpy surface" is a well-
known feature of mature clouds from constant bubbling (Mecikalski and Bedka, 2006). Existing algorithms used
Overshooting Top (OT) features in such clouds. There are two approaches to detect OTs: the brightness temperature
difference method and the infrared window-texture method (Ai et al., 2017). The brightness temperature difference method
uses a difference in T_b between the water vapor (WV) channel and IR window channel ($T_{b,wv} - T_{b,IR}$). Positive values of $T_{b,wv}$
$- T_{b,IR}$ due to the forcing of warm WV from below into the lower stratosphere are used as an indicator of OTs (Setvak et al.,
2007). However, since the threshold for the difference between two channels can depend on several factors, Bedka et al.
(2010) suggested another method to detect OTs which is called the Infrared window-texture method. This method takes
advantage of a feature of OT that it is an isolated region with cold T_b surrounded by relatively warm anvil region (Bedka et
al., 2010). This method, unfortunately, cannot avoid having to choose T_b thresholds that vary according to seasons or regions
(Dworak et al., 2012). Bedka et al. 2016 tried to minimize the use of fixed detection criteria. They developed two OT
detection algorithms based on IR and VIS channels, and an OT probability was produced through a pattern-recognition
scheme. The pattern-recognition scheme using VIS channels uses visible texture caused by strong updrafts.

The use of VIS and IR sensors in detecting convection can benefit significantly with the launch of National Oceanic and
Atmospheric Administration's (NOAA's) Geostationary Operational Environmental Satellites (GOES) – R Series which has
high resolution, rapidly updating (i.e. 1 minute) imagery. This study makes use of this new data, namely the 1 minute data
available from GOES-16 and GOES-17 in "mesoscale sectors" to update methods for detecting convection in different
stages. One is developed for CI using T_b from an IR channel in GOES-R. As in previous papers by Mecikalski and Bedka
(2006) or Mecikalski et al. (2010), temporal trends of the data were used but, since GOES-R has high temporal resolution, ten
consecutive data with 1-minute interval were used. This procedure eliminates errors from cloud movements that needed to be
dealt with in previous studies. Another one is developed for mature convection using both reflectances from a VIS channel
and T_b. For this algorithm, lumpy and rapidly changing surface and high cloud top height from mature convective clouds
were used to detect clouds both with and without OTs. These two methods were then combined to provide detection of
convection in all stages. The above methods are not intended to replace ground-based radars where these are available.
Instead, the focus here is complementing ground-based networks, either off-shore or other regions lacking coverage.

The datasets that were used to detect convection and validate the results are described in Sect. 2, while the methods used to identify initial and established convection are explained in Sect. 3. Sect. 4 highlights the results of each method. Two case

100 studies were examined followed by a one-month statistical study to quantify the operational accuracy of the methods.

2 Data

2.1 The Geostationary Operational Environmental Satellite R series (GOES-R)

Earth-pointing instruments of GOES-R consist of the Advanced Baseline Imager (ABI) with 16 channels, and the Geostationary Lightning Mapper (GOES-R Series Data Book, 2019). GOES-16 is the first of the two GOES-R series

105 satellites to provide data for severe weather forecast over the United States and surrounding oceans (Smith et al., 2017). Both T_b and reflectance data from the ABI were used to detect convective regions. Spatial and temporal resolutions of the GOES-16 data are summarized in table 1. Mesoscale data with one minute temporal resolution were used to fully exploit its high temporal resolution of the new instrument.

110 Reflectance at 0.64μm (Channel 2) and T_b at 6.2μm (Channel 8), 7.3μm (Channel 10), and 11.2μm (Channel 14) were used in the study. Channel 2 is a "red" band with the finest spatial resolution of 0.5km. This fine spatial resolution is useful to resolve lumpy, or bubbling surfaces of clouds in their mature stage. Channel 2 reflectance data were normalized by solar zenith angle so that a single threshold can be used throughout the method regardless of locations of the sun. Channel 14 is an IR longwave window band, which is a good indicator of the cloud top temperature for cumulonimbus clouds (Müller et al.,

115 2018). High reflectance and texture of the cloud top seen in channel 2 and cloud top height inferred from channel 14 are combined to determine locations of mature convective clouds.

Channel 8 and 10 are ABI water vapor channels with 2km spatial resolution. Because Channel 8 sees WV at somewhat higher altitudes than Channel 10, they can observe WV associated with updrafts as they progress upwards, and were therefore

120 used to detect early convection.

2.2 NEXRAD and MRMS

Multi-Radar/Multi-Sensor (MRMS) data developed at NOAA's National Severe Storms Laboratory were used for validation purposes. MRMS integrates the radar mosaic from the Next Generation Weather Radar (NEXRAD) with atmospheric environmental data, satellite data, lightning, and rain gauge observations to produce three dimensional fields of precipitation

125 (Zhang et al., 2016). These quantitative precipitation estimation (QPE) products have a spatial resolution of 1km and temporal resolution of 2 minutes.

A "PrecipFlag" variable contained in the standard MRMS product classifies precipitating pixels into seven categories: 1) warm stratiform rain, 2) cool stratiform rain, 3) convective rain, 4) tropical–stratiform rain mix, 5) tropical–convective rain

130   mix, 6) hail, and 7) snow. Details of the classification can be found in Zhang et al. (2016). A reduced set of these classes were used to validate the convective classification from GOES ABI data. In this study, warm stratiform rain, cool stratiform rain, and tropical-stratiform rain mix are all assigned a stratiform rain type while grids with convective rain, tropical-convective rain mix, and hail are assigned a convective rain type. Along with the classification product, MRMS provides a variable called "Radar QPE quality index (RQI)". This product is associated with quality of the radar data, which is a

135   combination of errors coming from beam blockages and the beam spreading/ascending with range (Zhang et al., 2016). This flag is used to mask out regions with low radar data quality. Only data with RQI greater than 0.5 are used in this study.

3 Methodology

This study examines methods to detect convective clouds at each life stage. Convective clouds can be divided into actively growing clouds and mature clouds. Actively growing clouds are usually clouds at the initial stage that grow nearly vertically

140   while mature clouds are capped, but continue to bubble due to the release of latent heat. They often move horizontally after they reach the tropopause. The proposed method to detect actively growing cloud is similar to the GOES-R CI algorithm in the sense that the method uses temporal trends of T_b. The availability of higher temporal resolution data, however, allows us to simplify the method somewhat to use only two channels in the water vapor absorption band. The high temporal resolution data further simplifies the method because the use of derived wind motion in tracking clouds is no longer necessary. One

145   minute is short enough that cloud motion, at most, is to the adjacent grids, and clouds can be easily tracked by focusing on overlapped scenes.

The method to detect mature convective clouds is similar to previous studies by Bedka et al. 2016 and Bedka et al. 2019 in terms of using the texture of the cloud top surfaces to infer strong updrafts. Cloud top surfaces of mature convective clouds

150   are much bumpier than any other clouds, and their bumpiness is most evident in VIS images with the finest resolution. The following method uses horizontal gradients of reflectance to represent the bumpiness of cloud tops, and the magnitude of the gradients are used to distinguish convective cores from their anvil clouds. Cloud top temperatures from channel 14 are used to eliminate low cumulus clouds that might appear bubbling.

3.1 Detection of actively growing clouds with brightness temperature data

155   In the early stage of convection, updrafts of water vapor eventually lead to condensation, the release of latent heat, and convective processes. Operational weather radars cannot observe this, but GOES-ABI, with water vapor absorption bands, can. During the early convective stages, T_bs that are sensitive to water vapor will decrease due to the increasing height (and cooler temperature) of water vapor and cloud droplets. Two ABI channels around the water vapor absorption bands, channel 8 (6.2µm) and channel 10 (7.3µm), were selected to cover water vapor updrafts at different height levels. These channels

160   were used to find small regions consistent with developing clouds. If a cloud develops continuously for ten minutes and shows a large decrease in T_b over ten minutes in either channel, the cloud is determined to be convective.

To compute the T_b decrease in clouds, a window has to be defined as it is usually difficult to precisely define the boundary of clouds, especially at the early stages of convection. Since most of the early convective clouds are smaller than 10km in

165   diameter, the window was defined as a 10km×10km box which is essentially a 5×5 matrix of satellite pixels consisting of 25 T_bs with 2km resolution. Considering the fact that a convective core usually has the lowest T_b within its neighborhood, the T_b matrix was formed around a pixel only if that pixel had the lowest T_b in the 5×5 matrix. However, this criterion alone could not distinguish convective cores from stratiform clouds and cloud edges which can also exhibit a local minimum. In addition to the lowest T_b, the shape of convective clouds is therefore also considered. As shown in the Fig. 1a, convective clouds not

170   only have the lowest T_b in their cores in all directions, but also have increasing T_bs away from the core, making their T_b distributions look like an inverted two-dimensional (2D) Gaussian distribution. To select T_b matrices that have this inverted Gaussian shape, an inverted 5×5 Gaussian matrix that has mean and standard deviation of the T_b matrix was created and compared with the T_b matrices. To focus the comparisons on the shape of the T_b distribution (Fig. 1b), the maximum T_b found in the 5×5 matrix was subtracted from all values, and T_b values were divided by the difference between maximum and

175   minimum T_b to normalize the T_b matrix itself. If the T_b matrix has a shape of a developing cloud (i.e. 2D inverse Gaussian), the absolute value of the difference between two matrices will be small. A threshold of 10 for this absolute value of the difference between T_b shape and inverse Gaussian shape (sum of residuals between normalized T_b and inverse Gaussian) was empirically determined to exclude non-convective scenes. T_b matrices with values greater than 10 are removed from the scene. This is done for all ten consecutive T_b images that are one minute apart. Continuous overlaps of T_b matrices for ten

180   minutes imply that the cloud maintained a convective shape for ten minutes, and therefore, changes in T_b are calculated to assess if the cloud in the T_b matrices was growing.

The minimum T_bs of the T_b matrices at each time step were linearly regressed against time to measure a decreasing trend. Since one-minute data can be noisy, the decreasing trend was considered instead of an actual difference in T_b during

185   10minutes. If the fitted line had a slope smaller than -1K/min for channel 10 or -0.5K/min for channel 8, the grid with the lowest T_b at each time step for ten minutes as well as the neighboring 8 grids in the window were classified as convective. The threshold of -1K/min and -0.5K/min were determined empirically, although it might not be the perfect threshold. Some convective clouds in the early stage show smaller decreasing trend, but using a smaller value for the threshold can introduce clouds that do not grow into deep convective clouds in the end. Clouds that develop into deep convective clouds are

190   eventually captured by these thresholds in later times even if they had small decrease in the beginning. Actively growing clouds are usually detected by channel 10 first and then by channel 8. This makes sense because channel 10 sees water vapor

in lower parts of the atmosphere while channel 8 sees upper level water vapor. Using two channels help find the same clouds in different levels.

3.2 Detection of mature convective clouds with reflectance data

195 Mature convective clouds consist of convective cores and stratiform or cirrus regions where clouds have detrained from the core. The lack of discrete boundaries between different types of clouds make it difficult to separate convective grids from surrounding stratiform regions. Overshooting tops and enhanced-V pattern are well-known features in mature convective clouds, but these do not appear until their strongest stage and not in all convective clouds. Using such features associated with the deepest convective cores will create a detection gap between early and mature stages of convection. The method

200 described here tries to minimize the gap, while still accurately detecting convective clouds.

A distinct feature that appears in convective clouds, even in their early stages, is a bubbling cloud top. The lumpiness of cloud tops can be numerically represented by calculating horizontal gradients in the reflectance field with the Sobel-Feldman (Sobel) operator which is commonly used in edge detection. The horizontal gradient is calculated at each pixel. The Sobel

205 operator convolves the target pixel and its surrounding eight grids with two kernels given in Eq. (1) to produce gradients in the horizontal and vertical direction.

$$G_x = \begin{bmatrix} +1 & 0 & -1 \\ +2 & 0 & -2 \\ +1 & 0 & -1 \end{bmatrix} \quad G_y = \begin{bmatrix} +1 & +2 & +1 \\ 0 & 0 & 0 \\ -1 & -2 & -1 \end{bmatrix} \qquad (1)$$

210 By using Eq. (2), gradients in each direction are combined to provide the absolute magnitude of the gradient at each point.

$$\text{Magnitude of gradient} = \sqrt{G_x^2 + G_y^2} \qquad (2)$$

Flat surfaces will have low gradients while cloud edges or lumpy surfaces will have high gradients. This lumpy feature is most evident in a VIS channel with the finest spatial resolution of 0.5km. IR fields are not very useful as the brightness

215 temperature variations in these lumpy surfaces tend to be quite small relative to the IR's 2km resolution, and only cloud edges stand out.

Before evaluating the texturs, only the grids that are potentially parts of deep convection are selected using simple threshold values of VIS (ABI channel 2; 0.65µm) and IR (ABI channel 14; 11.2µm) channels. Channel 2 reflectance is highly

220 correlated with the cloud optical depth (Minnis and Heck, 2012) while Channel 14 brightness temperature is related to cloud top temperature (Müller et al., 2018). These channels are used in GOES-R baseline product retrieval of cloud optical depth

and cloud top properties, respectively. Any grids with reflectance less than 0.8 or T_b greater than 250K during ten time steps (10 minutes) are removed since they generally represent thin or low clouds such as cirrus or growing clouds that can be identified by the CI method described earlier. These thresholds are chosen rather generously to include some convective
225   clouds that have not grown into deep convection yet, while still avoiding the misclassification of low cumulus clouds and thin anvil clouds as convective. The threshold of 250K is much warmer than typical values used in detecting deep convective features such as overshooting tops (Bedka et al., 2010) or enhanced-V (Brunner et al., 2007). It is intentionally chosen so that the method considers warmer convective clouds without those features in the next step when evaluating lumpiness of cloud top. The choice of these thresholds is discussed in more detail in section 4.3.

230

Once cold, highly reflective scenes are identified, the horizontal gradients of reflectance are calculated using the Sobel operator. The average of the horizontal gradients over the ten 1-minute time steps is calculated for each grid, and grids are removed if the average was less than 0.4 or greater than 0.9. Values below 0.4 or above 0.9 generally implies either stratiform region with a flat surface or cloud edges with very high gradients. The remaining grids were then interpolated into 1km maps
235   to be consistent with the spatial resolution of MRMS dataset. Neighboring grids were grouped to form clusters, and only the clusters with more than 5 grid points were assigned as a mature convective cloud to remove noise.

4 Results

We begin the result section with two case studies that illustrate the technique as well as some of its limitations.

4.1 June 28th, 2017

240   Supercell thunderstorms developed in Iowa and produced several tornado touchdowns. In Fig. 2a, deep convection had already developed over central Iowa at 19:30UTC, and two convective cells in the red box started to develop in southeast Iowa, although they do not stand out from surrounding low clouds in the VIS image. These two convective clouds became parts of major storm system that formed around 21:30UTC, producing the tornadoes (Fig. 2b) in the area. The two cells appeared in the Omaha (KOAX), Des Moines (KDMX), and La Crosse (KARX) NEXRAD radars at 19:30UTC (Fig. 2c), but
245   reflectivity was very weak ($\leq$ 30dBZ). In addition, the MRMS PrecipFlag product is shown in Fig. 2d. Convection is colored in pink and stratiform in green. Although deep convections over central and northeast part of Iowa were assigned as convective in MRMS at 19:30UTC, the two growing clouds in the red box in Fig. 2a were not assigned convective flag until 19:48UTC.

250   Figure 3a shows brightness temperatures for ABI channel 10 at 19:27UTC. The two growing convective cells in the white circle are shown in barely visible yellow surrounded by high T_bs. The one on the left was detected using 10-minute data from 19:25UTC, but since both clouds were detected starting at 19:27UTC, a scene from 19:27UTC was used to demonstrate the method. Figure 3c and 3d show T_b matrices that exhibited the correct shape for developing cells (Gaussian shape) at

19:27UTC and 19:36UTC. However, not all of the matrices in these figures showed the evolution of the developing cells

255 (decreasing minimum T_b over 10K) between the two time steps. The only two matrices in this scene that satisfied both criteria of maintaining the shape of developing cells and growing vertically over ten time steps were the two in blue circles. These two matrices contain early convective clouds that grow into deep convection shown in Fig. 2b, and they are correctly captured by this method. Since the same method is used in each time step, the same window can be captured throughout an overlapping time period despite the starting time. Therefore, this method can be used continuously in time.

260

Results for the detection of mature convective clouds are shown in a step by step fashion in Fig. 4. Figure 4a is the same as in Fig. 2a, but is mapped using a different color table for better comparisons between steps. Figure 4b shows the pixels retained after eliminating all the grids that did not meet the reflectance and T_b thresholds (minimum reflectance over ten time steps greater than 0.8 and maximum T_b over ten time steps less than 250K). Figure 4c shows the horizontal gradient values after

265 applying the Sobel operator. The colorbar is set to be within the range of 0.4 and 0.9 to display potential convective regions that passed these thresholds in colors. White regions are either regions that have average gradients greater than 0.9 such as cloud edges or thin cirrus clouds, or regions that have average gradients less than 0.4 such as clear sky or stratiform regions. Eventually, only the regions that meet both the criteria in Fig. 4b and 4c are assigned to convection, and shown as white shade in Fig. 4d. When the locations of convective regions in Fig. 4c and 4d were parallax corrected with a constant cloud

270 top height of 10km and compared to retrieved products from radars in Fig. 2c and 2d, most of convective regions align well with high reflectivity regions in Fig. 2c and convective regions in Fig. 2d. However, a straight line around 44N at the right edge of Fig. 4d is definitely not a convective region, and it is due to unrealistically high reflectance in the raw satellite dataset. These kinds of artifacts were removed later in section 4.3 when the method was applied to a full month of data. However, multiple lines are difficult to remove at this stage in the processing and will result in false alarm. As quality control

275 procedures on ABI are improved, this may no longer be a source of significant errors.

4.2 June 18th, 2018

Another case was examined to evaluate the methods under different conditions. Severe storms developed over the Great Plains in June 18th, 2018, producing hail on the ground. At 22:30UTC, sporadic storms across Kansas and Oklahoma were observed by GOES-16. This scene contains both growing and mature convective clouds, and MRMS PrecipFlag for the scene

280 is shown in Fig. 5a and 5b. Green color represents stratiform and pink color represents convective clouds. Figure 5c and 5d are brightness temperature maps of the same scene at 22:30UTC and 22:40UTC, respectively. Growing clouds are shown in purple, blue, yellow, and green boxes. Convection in the purple box is detected using ten consecutive T_b data starting at 22:19UTC. Considering the last data used at 22:28UTC, it was detected six minute earlier than MRMS detection which was at 22:34UTC. The growing cloud in the blue box was detected 7 minute after MRMS detection at 22:38UTC. This cloud did

285 not grow rapidly enough and did not meet the T_b threshold for channel 10 at the onset of convection. However, it was detected by channel 8 as it grew higher altitudes. Similarly, a cloud in the green box was detected by channel 8 starting at

22:27UTC. Although it precipitated, this cloud did not grow into a severe storm. The growing cloud in the yellow box was detected by GOES using data from 22:29UTC and detected by MRMS at 22:38UTC. These results show that even though the thresholds for the T_b method can be strict for some growing clouds, the thresholds were adequate for detecting convective

290   storms in their earliest stages.

Black regions superimposed on the brightness temperature map in Fig. 5c represent convective regions identified by the mature convection method. There are slight misalignments of detected convective clouds between MRMS PrecipFlag products and GOES results possibly due to sheared vertical structures of the storms, but overall, they seem to match well.

4.3 Statistical results with one-month data

Thresholds used in the two case studies were chosen based on experiments applied to one month of data during June of 2017. The T_b method for detecting early convection only requires one threshold of T_b decrease. However, since water vapor channels have different sensitivity to water vapor, different values for the threshold are required for each channel (channel 8 and 10). Since clouds do not grow at the same speed, and growth rate can vary at different evolution stages, it is important to

300   find an appropriate threshold that best represents growth rate for clouds in their early stages. In order to investigate proper values, the 5×5 T_b windows that maintained the developing shape and had a decreasing trend of T_b during ten minutes are collected over the one month period. A total of 27971 and 73204 (for channel 8 and 10, respectively) 5×5 windows were collected, and precipitation types from MRMS were assigned for each window. Future MRMS convective flags up to 30 minutes were included in the analysis because some time delays were observed in MRMS product when assigning convective

305   flags, especially for early convection. When comparing GOES products to future MRMS products, future locations of GOES products were calculated assuming convection moves at a constant speed. Tables 2 and 3 show results applying different thresholds ranging from -0.1K/min to -2.0K/min. Numbers in the table represent the number of 5×5 windows that MRMS precipitation flags were assigned to either non-convective or convective at the corresponding 10-minute time window, as well as pixels that were flagged as convective by MRMS in the next 20 minutes to account for the fact that GOES can detect

310   convection before the radar sees precipitation. For channel 8, using a threshold less than -1.4K/min has 100% accuracy, but in return, it misses much of the convection and loses an ability to detect convection earlier than radar because most of early convection does not have such a strong updraft. Thresholds are chosen so that it achieves at least 85% accuracy and detects reasonable amounts of convections. Therefore, -0.5K/min and -1.0K/min are chosen for channel 8 and 10, respectively. It is interesting to note that some clouds did not produce precipitation even with rapid growth over -2.0K/min (for channel 10).

315   This could be because evaporation occurred while it fell, leading to virga, or it did not have enough time to grow bigger due to such a strong updraft.

The reflectance method used to identify mature convection uses three thresholds; reflectance at channel 2 and T_b at channel 14 to remove shallow and low clouds, and horizontal gradients of reflectance at channel 2 to remove cloud edges as well as

320   clouds with flat cloud top surfaces. Cloud top texture (horizontal gradients of reflectance) is the key feature to detect convection in this method, but since low cumulus clouds can also have lumpy cloud top surfaces, reflectance and T_b thresholds are used additionally to distinguish these low or shallow cumulus clouds from convective clouds.

Results using different combinations of the three thresholds are compared. First, the lower bound of the texture thresholds are
325   varied, keeping the upper threshold and the T_b and reflectance thresholds constant. Resulting FAR and POD are shown in Fig. 6. The upper threshold does not change results much, and cloud edges are effectively removed by the threshold of 0.9. Using 0.5 (yellow) misses significant amounts of convective regions while using lower values (blue and red) substantially misclassifies stratiform regions with flat cloud tops as convective, although their PODs are much higher. A value of 0.4 (green diamond in Fig. 6) was chosen as a reasonable compromise between POD and FAR.

330

POD and FAR using different combinations of T_b and reflectance thresholds are plotted in Fig. 7, and this time texture thresholds are kept constant with 0.4 and 0.9. The T_b threshold is varied from 230K to 250K, and the reflectance threshold is varied from 0.7 to 0.9. There is a trade-off between detecting more mature convective clouds in the earlier stage and incorrectly assigning cumulus clouds as convective clouds. Having lower value for the T_b threshold or higher value for the
335   reflectance threshold leads to small FAR, but also leads to small POD. To make this method effective and not too harmful for the data assimilation, 250K for the T_b and 0.8 for the reflectance threshold (black diamond in Fig. 7a) are chosen. 240K and 0.7 (orange) also showed similar results, but 250K and 0.8 were chosen due to lower FAR. Figure 7b shows results including MRMS data 10 minutes after the detection period to show its ability to detect convection earlier than MRMS. Most of the results showed improvements in both FAR and POD (lower FAR and higher POD) when later data are included.

340

Despite FAR being relatively small, the method misses significant amounts of convective areas observed by MRMS. Therefore, regions that were missed are evaluated further to investigate which threshold was most effective in preventing the method from detecting convective regions. Figure 8 shows histograms of T_b, reflectance, and texture in the convective regions that were missed by the above method. It is clear from the figure that the largest number of misses were due to low
345   texture values. There are many reasons why convective regions appear to have flat cloud top surfaces. Anvil or thick cirrus clouds above convective regions can smooth out or cover bubbling cloud tops, and there is simply no way to avoid this problem. Another reason may be the nature of the classification method. Since classification by MRMS is determined by rain rate, even if convective clouds are in a decaying mode and do not bubble anymore, clouds can still continue to precipitate considerable amounts, which would lead to convective category in the MRMS product. It is also possible that it is due to a
350   misclassification of trailing stratiform regions using radars. Previous studies (Qi et al. 2013; Shusse et al. 2011) have indeed tried to improve the radar classification schemes.

As shown from these results, there are no perfect thresholds that can separate convective and stratiform clouds. Nevertheless, threshold values were chosen based on our purpose, which are to avoid FAR as much as possible and have decent POD comparable to radar products. Results applying both methods to one month data with the chosen thresholds are summarized in table 4, and based on the table, FAR is 14.4% and POD is 45.3%. Most of the detection was from mature convective clouds, and its accuracy of 85.8% was much higher than that of the detection of growing clouds, which was 71.0% at a pixel level. When MRMS data up to 30 minutes were included in the analysis, considering methods' ability to detect convection earlier than radar, the accuracy of both methods increased, and overall FAR was reduced to 11.2%. Although FAR is slightly over 10%, 96.4% of these pixels were at least raining. Since the main objective of data assimilation is to have good prediction of precipitation, applying these methods during data assimilation can still be beneficial in case the forecast model did not produce precipitation.

5 Conclusion and summary

This study explores two methods to detect convective clouds using GOES-R ABI data with one minute interval. Using such high temporal resolution data facilitates cloud tracking and helps the accuracy of the detection method when calculating decreases in T_b of the same cloud. Convective clouds in the early stage were detected using T_bs of ABI channels 8 and 10. These channels were used to find cloud scenes with the developing shape of convective clouds. They were then used again to calculate the T_b decrease for those which maintained the developing shape for ten minutes. A cloud scene that had a consistent developing shape and a large decrease in T_b over ten minutes was classified as convective by this method. Mature convective clouds were detected by masking out regions with high T_b in ABI channel 14 and low reflectance in ABI channel 2 and finding regions with high horizontal gradients of reflectance over the course of ten minutes. Results from this reflectance method were mostly consistent with the radar-derived products, although this method is limited to daytime use only. Nevertheless, it detects a wide range of convective area, not just regions with overshooting tops.

These methods work well for well-structured convective clouds, but there are limitations to this method as with most algorithms using IR and VIS sensors have. Cirrus cloud shields are the biggest problem as they block T_b decreases underneath and smooth out lumpy reflectance surfaces. However, these methods can still be extremely useful for defining convection for assimilation into models where radar data is not available. Because regions identified as convective are most likely convective (~90% accuracy), this can easily be assimilated while setting cloudy regions to "missing" since the accuracy of detecting convection under large cirrus shields is poor.

Author contributions

All three authors designed the experiments. YL processed and analysed the data. CK and MZ gave feedbacks with their insights at every step of the data analysis. The manuscript was written jointly by YL, CK, and MZ.

Competing interests

385   The authors declare that they have no conflicts of interests.

Data availability

NEXRAD reflectivity data were obtained by NOAA's National Centers for Environmental Information: doi:10.7289/V5W9574V. Past MRMS datasets are available at http://mtarchive.geol.iastate.edu/. GOES-R data were made available by Cooperative Institute for Research in the Atmosphere (CIRA).

390   **Acknowledgement**

This research is supported by CIRA's Graduate Student Support Program, as well as the WMO sponsored ICEPOP-18 project through the Korean Meteorological Administration.

References

Ai, Y., Li, J., Shi, W., Schmit, T. J., Cao, C., and Li, W.: Deep convective cloud characterizations from both broadband
395   imager and hyperspectral infrared sounder measurements, J. Geophys. Res., 112, 1700-1712, doi: 10.1002/2016JD025408, 2017.

Bauer, P., Thorpe, A., and Brunet, G.: The quiet revolution of numerical weather prediction, Nature, 525, 47-55, doi: 10.1038/nature14956, 2015.

Bedka, K., Brunner, J., Dworak, R., Feltz, W., Otkin, J., and Greenwald, T.: Objective satellite-based detection of
400   overshooting tops using infrared window channel brightness temperature gradients, J. Appl. Meteorol., 49, 181-202, doi: 10.1175/2009JAMC2286.1, 2010.

Bedka, K. and Khlopenkov, K.: A probabilistic multispectral pattern recognition method for detection of overshooting cloud tops using passive satellite imager observations, J. Appl. Meteorol. Climatol., 55, 1983-2005, doi: 10.1175/JAMC-D-15-0249.1, 2016.

405   Benjamin, S. G., Weygandt, S. S., Brown, J. M., Hu, M., Alexander, C. R., Smirnova, T. G., Olson, J. B., James, E. P., Dowell, D. C., Grell, G. A., Lin, H., Peckham, S. E., Smith, T. L., Moninger, W. R., Kenyon, J. S., and Manakin, G. S.: A North American hourly assimilation and model forecast cycle: The rapid refresh, Mon. Weather. Rev., 144, 1669-1694, doi: 10.1175/MWR-D-15-0242.1, 2016.

Bonavita, M., Trémolet, Y., Holm, E., Lang, S. T. K., Chrust, M., Janisková, M., Lopez, P., Laloyaux, P., de Rosnay, P.,
410   Fisher, M., Hamrud, M., and English, S.: A Strategy for Data Assimilation. Technical Memo. 800. ECMWF: Reading, UK, 2017.

Brunner, J. C., Ackerman, S. A., Bachmeier, A. S., and Rabin, R. M.: A quantitative analysis of the enhanced-V feature in relation to severe weather, Weather and Forecasting, 22, 853-872, doi: 10.1175/WAF1022.1, 2007.

Weygandt, S. S., Alexander, C. R., Dowell, D. C., Hu, M., James, E. P., Benjamin, S. G., Smirnova, T. G., Lin, H., Kenyon,
415   J., and Olson, J. B.: Radar data assimilation impacts in the RAP and HRRR models, 20th Conf. on Integrated Observing and Assimilation Systems for the Atmosphere, Oceans, and Land Surface (IOAS-AOLS), New Orleans, Louisiana, United States, Amer. Meteor. Soc., 10-14 January 2016. Available online at
https://ams.confex.com/ams/96Annual/webprogram/Paper289787.html

Churchill, D. D. and Houze Jr, R. A.: Development and structure of winter monsoon cloud clusters on 10 December 1978. J.
420   Atmos. Sci., 41, 933-960, doi: 10.1175/1520-0469(1984)041<0933:DASOWM>2.0.CO;2, 1984.

Dworak, R., Bedka, K., Brunner, J., and Feltz, W.: Comparison between GOES-12 overshooting-top detections, WSR-88D radar reflectivity, and severe storm reports, Weather and Forecasting, 27, 684-699, doi: 10.1175/WAF-D-11-00070.1, 2012.

Geer, A., Ahlgrimm, M., Bechtold, P., Bonavita, M., Bormann, N., English, S., Fielding, M., Forbes, R., Hogan, R., Hólm, E., Janisková, M., Lonitz, K., Lopez, P., Matricardi, M., Sandu, I., and Weston, P.: Assimilating observations sensitive to
425   cloud and precipitation. Technical Memo. 815. ECMWF: Reading, UK, 2017.

GOES-R Series Data Book, 2019. Available from: https://www.goes-r.gov/resources/docs.html

Jones, T. A., Knopfmeier, K., Wheatley, D., Creager, G., Minnis, P., and Palikonda, R.: Storm-scale data assimilation and ensemble forecasting with the NSSL experimental warn-on-forecast system. Part II: Combined radar and satellite data experiments. Weather and Forecasting, 31, 297-327, doi: 10.1175/WAF-D-15-0107.1, 2016.

430   Mecikalski, J. R. and Bedka, K.: Forecasting convective initiation by monitoring the evolution of moving cumulus in daytime GOES imagery. Mon. Weather Rev., 134, 49–78, doi: 10.1175/MWR3062.1, 2006.

Mecikalski, J. R., MacKenzie Jr, W. M., Koeing, M., and Muller, S.: Cloud-top properties of growing cumulus prior to convective initiation as measured by Meteosat Second Generation. Part I: Infrared fields. J. Appl. Meteor. Climatol. 49, 521-534, doi: 10.1175/2009JAMC2344.1, 2010.

435   Migliorini, S., Lorenc, A. C., and Bell, W.: A moisture-incrementing operator for the assimilation of humidity and cloud-sensitive observations: formulation and preliminary results. *Q. J. R. Meteorol. Soc*. 144, 443-457, 2018.

Minnis P. and Heck, P. W.: GOES-R Advanced Baseline Imager (ABI) Algorithm theoretical basis document for nighttime cloud optical depth, cloud particle size, cloud ice water path, and cloud liquid water path, 2012. Available from:
https://www.goes-r.gov/products/baseline-cloud-opt-depth.html

440   Müller, R., Haussler, S., and Jerg, M.: The role of NWP filter for the satellite based detection of cumulonimbus clouds. Remote Sens., 10(3), 386, doi: 10.3390/rs10030386, 2018.

Qi, Y., Zhang, J., and Zhang, P.: A real-time automated convective and stratiform precipitation segregation algorithm in native radar coordinates. Q.J.R. Meteorol. Soc., 139, 2233-2240, doi: 10.1002/qj.2095, 2013.

Setvák, M., Rabin, R. M., and Wang, P. K.: A real-time automated convective and stratiform precipitation segregation
445   algorithm in native radar coordinates. Q.J.R. Meteorol. Soc., 139, 2233-2240, doi: 10.1002/qj.2095, 2007.

Sieglaff, J. M., Cronce, L. M., Feltz, W. F., Bedka, K., Pavolonis, M. J., and Heidinger, A. K.: Nowcasting convective storm initiation using satellite-based box-averaged cloud-top cooling and cloud-type trends. J. Appl. Meteor. Climatol., 50, 110-126, doi: 10.1175/2010JAMC2496.1, 2011.

450   Sieglaff, J. M., Cronce, L. M., and Feltz, W. F.: Improving satellite-based convective cloud growth monitoring with visible optical depth retrievals. J. Appl. Meteor. Climatol, 53, 506-520, doi: 10.1175/JAMC-D-13-0139.1, 2014.

Smith, T. J., Griffith, P., Gunshor, M. M., Daniels, J. M., Goodman, S. J., and Lebair, W. J.: A closer look at the ABI on the GOES-R Series. Bull. Amer. Meteor. Soc., 98, 681-698, doi: 10.1175/BAMS-D-15-00230.1, 2017.

Steiner, M., Houze Jr, R. A., and Yuter, S. E.: Climatological characterization of three-dimensional storm structure from operational radar and rain gauge data. J. Appl. Meteor., 34, 1978-2007, doi: 10.1175/1520-

455   0450(1995)034<1978:CCOTDS>2.0.CO;2, 1995.

Tao, W-K, Simpson J., Lang, S., McCumber, M., Adler, R., and Penc, R.: An algorithm to estimate the heating budget from vertical hydrometeor profiles. J. Appl. Meteor, 29, 1232-1244, doi: 10.1175/1520-
0450(1990)029<1232:AATETH>2.0.CO;2,
1990.

460   Yano, J-I, Ziemiański, M. Z., Cullen, M., Termonia, P., Onvlee, J., Bengtsson, L., Carrassi, A., Davy, R., Deluca, A., Gray, S. L., Homar, V., Köhler, M., Krichak, S., Michaelides, S., Phillips, V. T. J., Soares, P. M. M., and Wzszogrodzki, A. A.: Scientific challenges of convective-scale numerical weather prediction. Bull. Amer. Meteor. Soc., 99, 699-710, doi: 10.1175/BAMS-D-17-0125.1, 2018.

Zhang, J., Langston, C., and Howard, K.: Brightband identification based on vertical profiles of reflectivity from the WSR-

465   88D. J. Atmos. Ocean. Technol., 25, 1859-1872, doi: 10.1175/2008JTECHA1039.1, 2008.

Zhang, J. and Qi, Y.: A real-time algorithm for the correction of brightband effects in radar-derived QPE. J. Hydrometeor., 11, 1157-1171, doi: 10.1175/2010JHM1201.1, 2010.

Zhang, J., Howard, K., Langston, C., Kaney, B., Qi, Y., Tang, L., Grams, H., Wang, Y., Cocks, S., Martinaitis, S., Arthur, A., Cooper, K., Brogden, J., and Kitzmiller, D.: Multi-Radar Multi-Sensor (MRMS) quantitative precipitation estimation: Initial

470   operating capabilities. Bull. Amer. Meteor. Soc., 97, 621-638, doi: 10.1175/BAMS-D-14-00174.1, 2016.

475

480
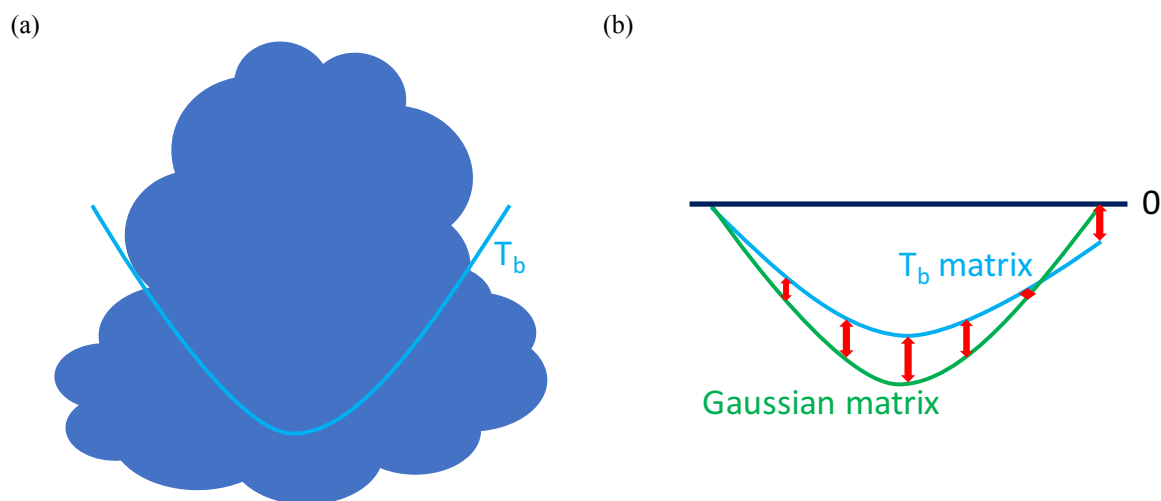
Figure 1: (a) A typical shape of a convective cloud and its T_b distribution around the convective core (blue line). (b) Schematic representation of distributions of the inverted Gaussian matrix (green) and the T_b matrix (blue) when the cloud is convective.

485

490
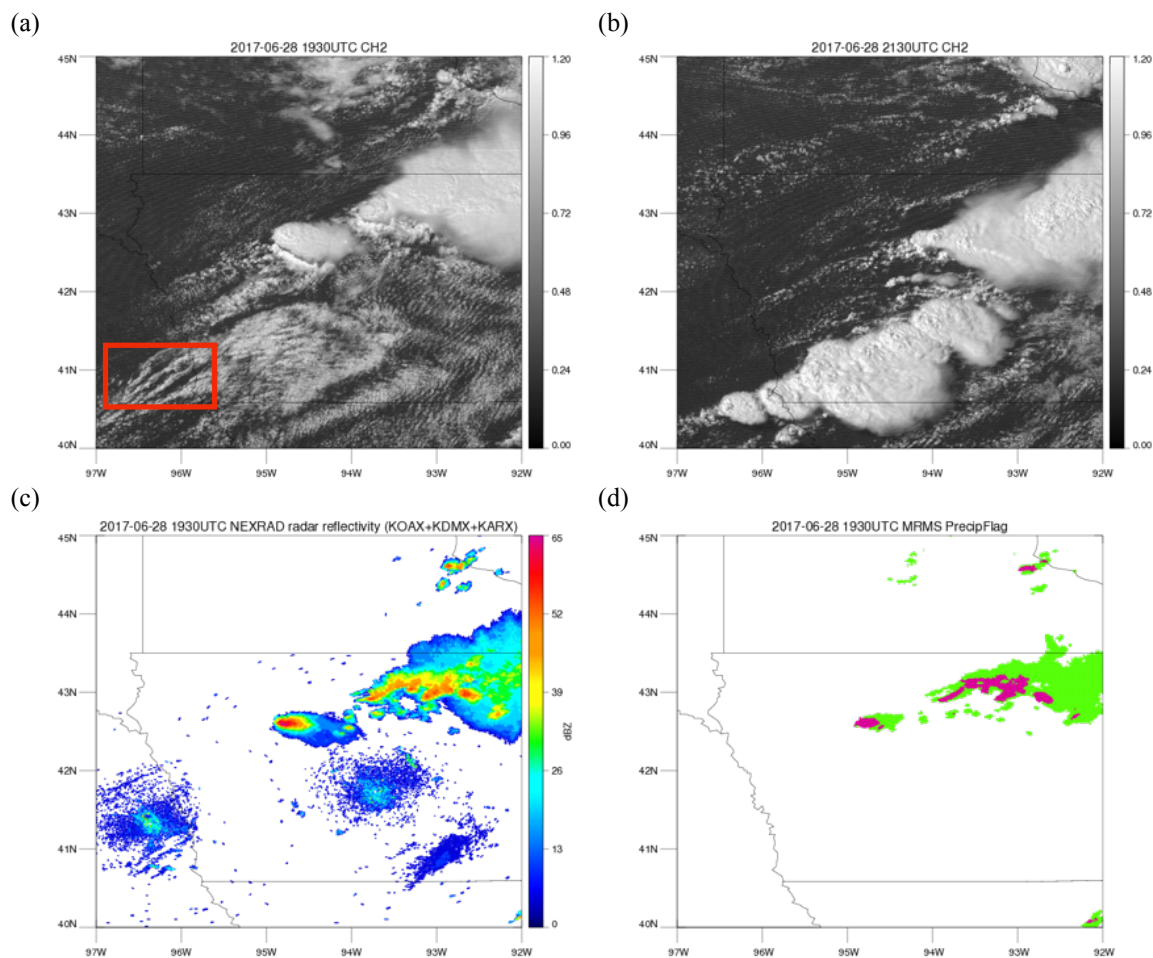
Figure 2: (a) GOES-ABI 0.65μm visible channel imagery (0.5km) at 1930UTC 28 June 2017 over Iowa. Numbers on the
495 **colorbar represent reflectances. The red box indicates regions where two convective cells are detected by the GOES T$_b$**
method. (b) GOES-ABI 0.65μm visible channel imagery at 2130UTC 28 June 2017. (c) NEXRAD composite reflectivity
(KOAX, KDMX, and KARX) around 1930UTC 28 June 2017. (d) MRMS PrecipFlag at 1930UTC 28 June 2017. Pink
represents convective while green represents stratiform.

500
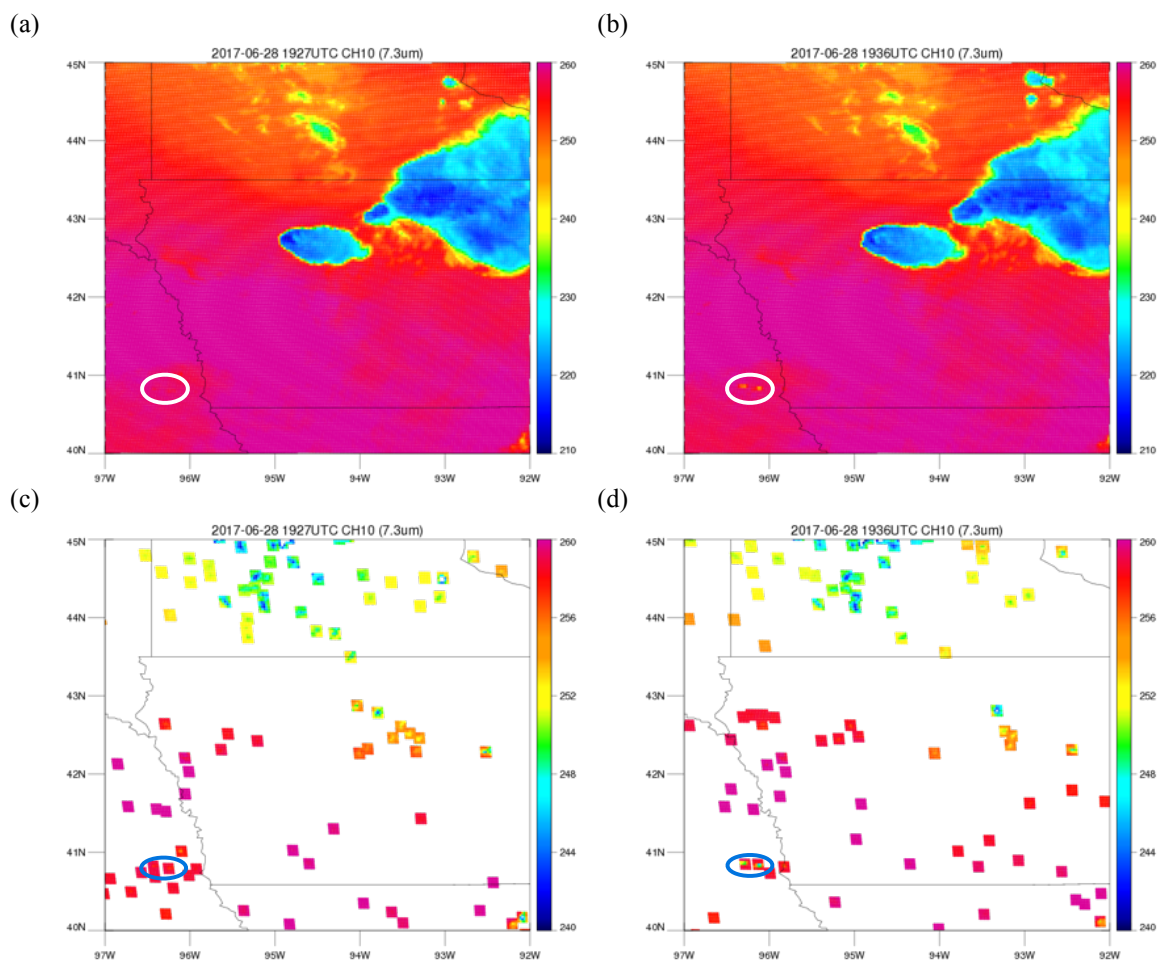
505 **Figure 3: (a) GOES-ABI 7.3μm infrared channel imagery (K) at 1927UTC 28 June 2017. White circle denotes regions where two convective clouds start to grow. (b) Same as figure 3a, but at 1936UTC. (c) T$_b$ matrices obtained from channel 10 (7.3μm) that have the Gaussian shape at 1927UTC 28 June 2017. Blue circle denotes the same region as the white circle in figure 3a. Note that the scale of the colorbar is adjusted from figure 3a and 3b to better observe convective initiation. (d) Same as figure 3c, but at 1936UTC.**

510

515
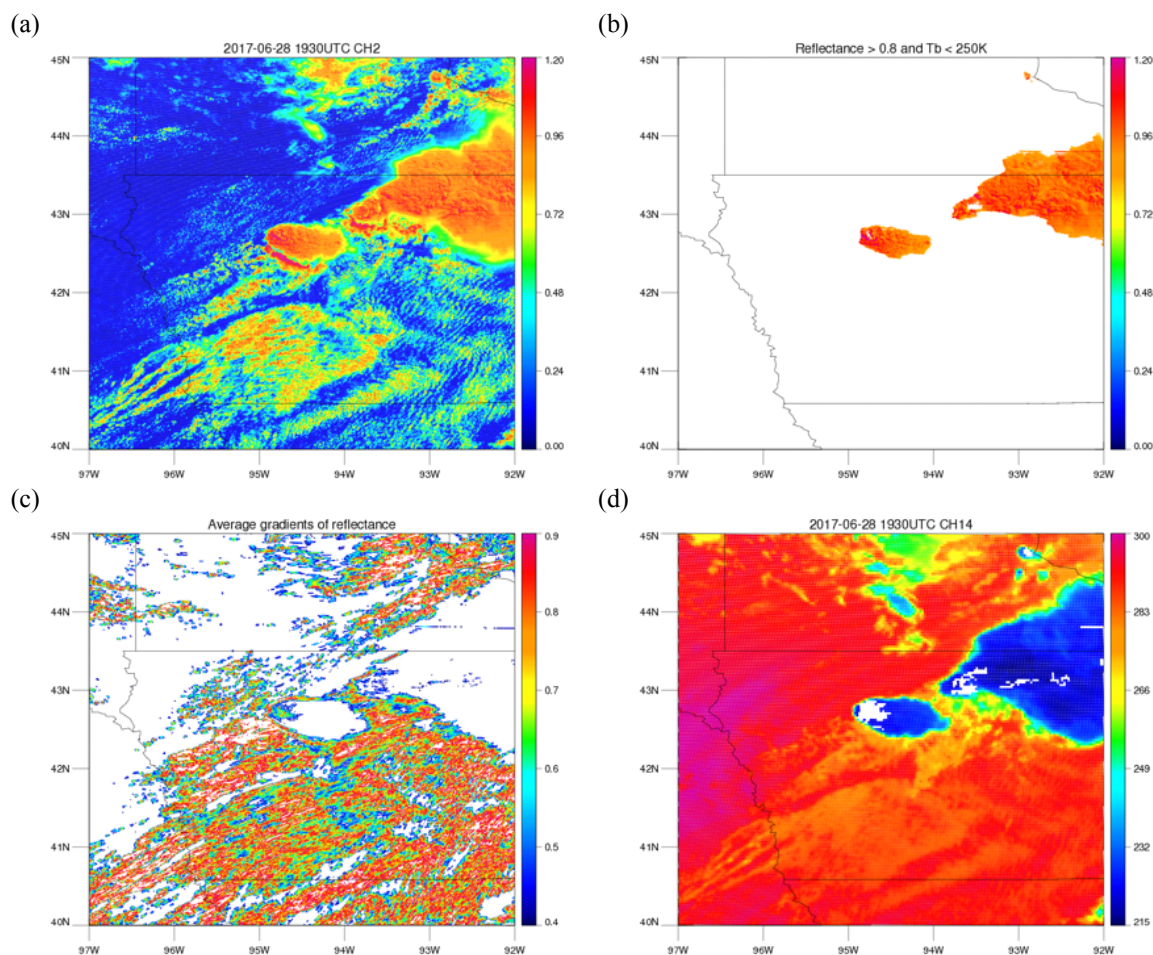
Figure 4: (a) Same as Figure 2a, but using different color table. (b) From the reflectance map in figure 4a, regions that have reflectances over 10 minutes less than 0.8 or have T_bs greater than 250K over 10 minutes are assigned reflectance of zero, and therefore colored in white. (c) Map of average gradients of reflectances over 10 minutes. Regions with average gradient less than 0.4 or greater than 0.9 are colored in white. (d) GOES-ABI 11.2μm infrared channel imagery (K) at 1930UTC 28 June 2017. Regions that passed two criteria from figure 4b and 4c are colored in white.
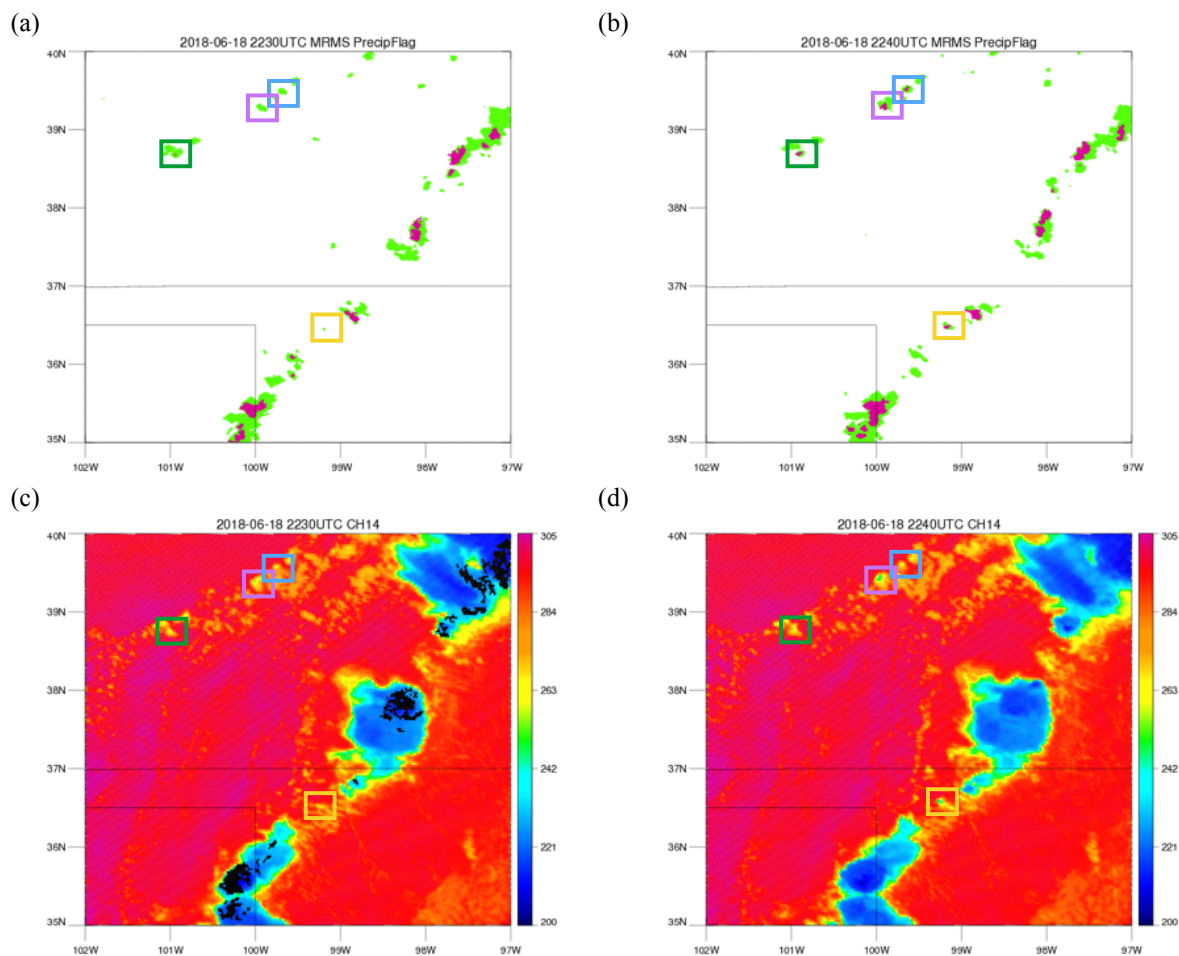
Figure 5: (a) MRMS PrecipFlag at 2230UTC 18 June 2018. Pink represents convective while green represents stratiform. (b) Same as figure 5a, but at 2240UTC. (c) GOES-ABI 11.2μm infrared channel imagery (K) at 2230UTC 18 June 2018 over the Great Plains. (d) Same as figure 5c, but at 2240UTC.

540
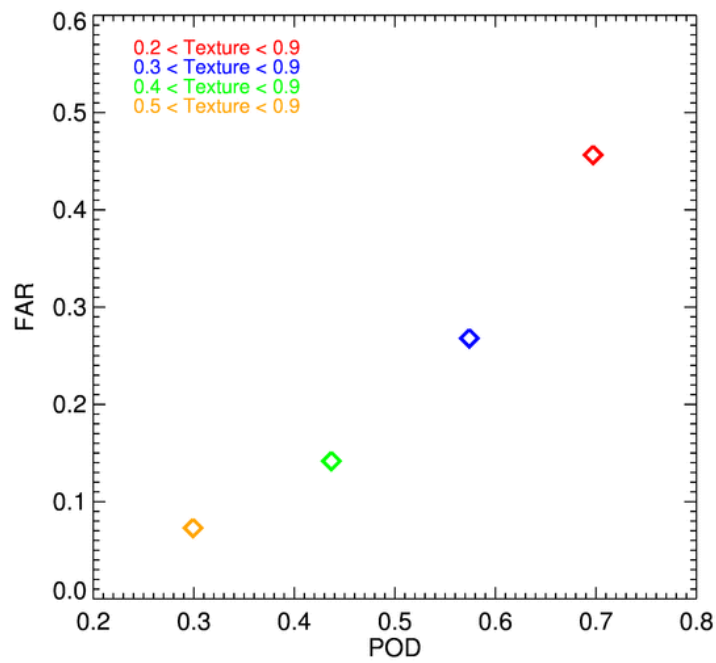
Figure 6: (a) Plot of probability of detection (POD) and false alarm ratio (FAR) using different texture thresholds.

545

550

(a) (b)
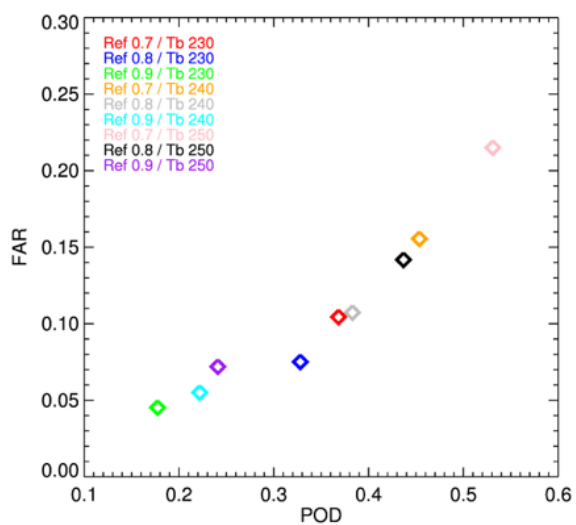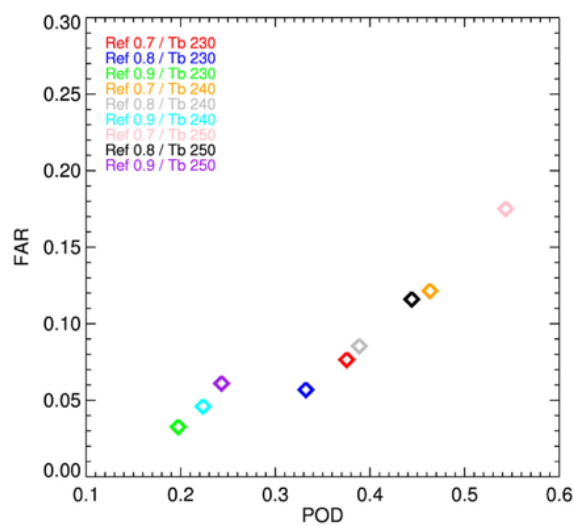
Figure 7: (a) Plot of probability of detection (POD) and false alarm ratio (FAR) for different combinations of T_b and reflectance thresholds. (b) Same as figure 7a, but including MRMS dataset 10 minutes after the detection period.

565
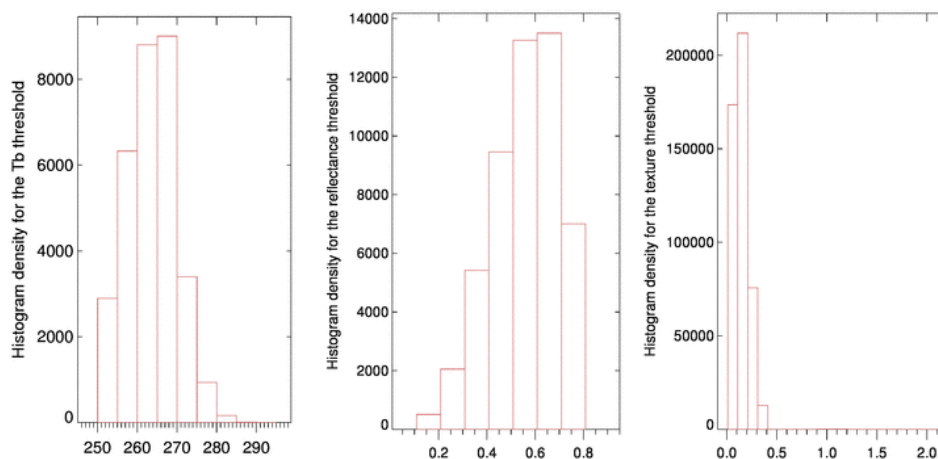
Figure 8: Histograms of T_b, reflectance, and texture values when the pixel was not detected by the GOES detecting
570 **method due to only one of the thresholds.**

575

580

Table 1. Spatial and temporal resolution of GOES-ABI

Spatial Resolution	
0.64μm visible	0.5km
Other visible/near-IR	1.0km
Bands (>2μm)	2km
Spatial Coverage	
Full Disk	4 per hour
Conus	12 per hour
Mesoscale	30 or 60 sec

Table 2. Number of non-convective, convective, convective within 10 minutes, and convective within 20 minutes for using
620 **different threshold values (channel 8)**

Threshold value (K/min)	Non-convective	Convective	Convective within 10 min	Convective within 20 min (overall accuracy)
-0.1	2635	1465	1610	1678 (38.9%)
-0.2	632	1099	1182	1212 (65.7%)
-0.3	269	848	913	933 (77.6%)
-0.4	137	664	706	715 (83.9%)
-0.5	83	531	561	568 (87.3%)
-0.6	47	443	468	473 (91.0%)
-0.7	27	354	375	378 (93.3%)
-0.8	15	290	305	308 (95.4%)
-0.9	11	233	246	249 (95.8%)
-1.0	7	190	202	204 (96.7%)
-1.1	7	162	171	173 (96.1%)
-1.2	3	133	139	141 (97.9%)
-1.3	1	105	108	109 (99.9%)
-1.4	0	80	83	84 (100.0%)
-1.5	0	64	66	67 (100.0%)
-1.6	0	53	55	55 (100.0%)
-1.7	0	44	46	46 (100.0%)
-1.8	0	35	36	36 (100.0%)
-1.9	0	28	28	28 (100.0%)
-2.0	0	21	21	21 (100.0%)

625

Table 3. Number of non-convective, convective, convective within 10 minutes, and convective within 20 minutes for using different threshold values (channel 10)

Threshold value (K/min)	Non-convective	Convective	Convective within 10 min	Convective within 20 min (overall accuracy)
-0.1	15444	2727	3228	3461 (18.3%)
-0.2	6110	2085	2377	2499 (29.0%)
-0.3	2862	1677	1869	1944 (40.4%)
-0.4	1443	1354	1477	1526 (51.4%)
-0.5	836	1126	1208	1241 (59.7%)
-0.6	520	947	1008	1031 (66.5%)
-0.7	305	794	839	856 (73.7%)
-0.8	211	666	701	713 (77.2%)
-0.9	135	562	587	597 (81.6%)
-1.0	86	475	497	504 (85.4%)
-1.1	57	406	426	433 (88.4%)
-1.2	40	339	354	359 (90.0%)
-1.3	27	276	289	293 (91.6%)
-1.4	20	244	256	259 (92.8%)
-1.5	13	196	207	209 (94.1%)
-1.6	6	179	189	191 (97.0%)
-1.7	5	151	160	161 (97.0%)
-1.8	4	131	136	137 (97.2%)
-1.9	3	108	112	112 (97.4%)
-2.0	2	90	94	94 (97.9%)

630